Materials Science and Engineering B 284 (2022) 115880

Contents lists available at ScienceDirect

Materials Science & Engineering B

journal homepage: www.elsevier.com/locate/mseb

Improved electrocatalytic properties of bundled B/N co-doped electrospun carbon nanofibers with Pt nanostructures through dopant-induced metal-support interaction (DIMSI)

Sathyanarayanan Shanmugapriya [a], Pei Zhu [b], Mariappan Ganeshbabu [a], Yun Sung Lee [c], Xiangwu Zhang [b], Ramakrishnan Kalai Selvan [a,b,*]

[a] Energy Storage and Conversion Devices Laboratory, Department of Physics, Bharathiar University, Coimbatore 641-046, Tamil Nadu, India
[b] Fiber and Polymer Science Program, Department of Textile Engineering Chemistry and Science, Wilson College of Textiles, North Carolina State University, Raleigh, NC 27695-8301, USA
[c] Department of Chemical Engineering, Chonnam National University, Gwangju 61186, Republic of Korea

ARTICLE INFO

Keywords:
Boron
Nitrogen
CNFs
Electrocatalyst
DIMSI

ABSTRACT

The dispersion of platinum nanoparticles over B/N functionalized carbon nanofibers (CNFs) is studied using a simple electrospinning technique. The ratio of boron and nitrogen for the uniform and agglomeration-free Pt loading is optimized. Among the prepared electrocatalysts, Pt-loaded CNFs with an equal amount of B and N (Pt/HCNF-III) exhibit remarkable electrocatalytic activity towards the oxygen reduction, methanol oxidation, and hydrogen evolution reactions. Pt/HCNF-III provides a significant ECSA (62.57 m^2/gm). The Pt/HCNF-III being an efficient ORR electrocatalyst follows a 4-electron pathway and renders high half-wave potential. Moreover, Pt/HCNF-III displays relatively high mass activities of 324.77 and 6.17 A g^{-1} during MOR and HER, respectively. Pt/HCNF-III also demands a minimal overpotential (54 mV) and Tafel slope (33 mV dec^{-1}) during HER. Thus, a unique phenomenon of dopant-induced metal support interaction has enhanced the electrocatalytic activity, stability, and selectivity of the prepared electrocatalysts.

1. Introduction

The dopant-induced metal-support interaction (DIMSI) is a critical phenomenon in the noble metal nanoparticles (NMNPs) dispersed heteroatom functionalized carbon supports. The heteroatoms are induced the structural defects, modified the local electron density, and interacted favorably with the dispersed NMNPs. Moreover, the established functional groups serve as preferential interactive sites for the dispersion of metal particles [1]. The heteroatom functionalized carbon supports with Pt loading have been extensively used in various electrochemical applications. Due to the strong metal-support interaction, the heteroatoms doped functionalized carbon overcome the platinum dissolution, particle detachment, agglomeration, and Ostwald ripening. Among the class of heteroatoms (O, N, S, B, P, and F), the atomic radii of boron and nitrogen almost matched with carbon; hence their incorporation into an sp^2 carbon network doesn't have adverse effects on the atomic arrangement of two-dimensional hexagonal lattices [2]. Besides, the doping of nitrogen alters the charge distribution of carbon, enhances the metal-support chemical binding, modifies the nucleation and growth kinetics of Pt NPs, and improves the intrinsic activity of Pt catalysts. The mentioned amendments lead to higher dispersion, smaller particle size, and enhanced durability of supported Pt electrocatalysts [3]. Similarly, boron doping significantly alters the surface properties of carbon supports by introducing defect sites into the carbon lattice. These defect sites act as nucleation spots during metal deposition and anchor metal nanoparticles providing a uniform distribution [4,5]. Significantly, the synergistic doping of B & N delivers better electrocatalytic performance than their single dopant counterparts [6]. The controlled particle size/distribution with increased conductivity and variation in acid-base properties enhance the catalytic activity of the Pt electrocatalysts supported on the heteroatom-doped carbon supports [5].

Among various carbonaceous materials, the carbon nanofibers are endowed with significant properties such as unique nanostructured morphology, tunable surface chemistry, high mechanical strength, excellent corrosion resistance, high specific surface area, and significant thermal and electrical conductivity. Thus, functionalizing the CNFs with

* Corresponding author.
E-mail address: selvankram@buc.edu.in (R. Kalai Selvan).

https://doi.org/10.1016/j.mseb.2022.115880
Received 11 January 2022; Received in revised form 11 May 2022; Accepted 14 July 2022
Available online 30 July 2022

heteroatoms imparts remarkable strength to the dispersion of noble metal NPs [6]. Though there were numerous reports on heteroatom-doped carbon materials [7–11], the study on heteroatom co-doped CNFs/carbon nanotubes (CNTs) as Pt supports for electrocatalytic applications is very few. Li et al. synthesized boron, nitrogen, and phosphorous doped CNFs by chemical vapor deposition of acetylene on electroless-plated copper foams. During the oxygen reduction reaction, the prepared Pt/CNF electrocatalyst displayed higher stability than the state-of-the-art electrocatalyst (Pt/C-JM) [12]. Through a dissolution-diffusion-precipitation process, Zhu et al. have directly grown B and N co-doped carbon nanofibers on a cobalt foil. The resultant Pt/BNCNFs have increased oxygen reduction activity and durability in $HClO_4$ solution over commercial Pt/C [3]. Overall, dissolution-diffusion-precipitation, chemical vapor deposition, and thermolysis techniques have been used to prepare carbon nanostructures. Likewise, the Pt loading was around 40 wt%, which is twice higher than that of the commercial Pt/C (20 wt%). Besides, the ORR activity of the prepared electrocatalysts has been discussed in detail.

In this line, a facile single pot electrospinning technique is employed to prepare B and N co-doped carbon nanofibers in the present work. Moreover, the composition of heteroatom (B, N) in the carbon support is varied and optimized the favorable ratio of boron and nitrogen (50:50) for obtaining the agglomeration-free adsorption of Pt nanoparticles on the CNFs. Significantly, the ultra-minimal loading (4.5 wt%) of Pt is used to balance the cost and inevitable electrocatalytic properties. Subsequently, the physicochemical properties of the prepared carbon supports and Pt-loaded electrocatalysts are studied in detail. Finally, the prepared Pt dispersed boron and nitrogen co-doped carbon nanofibers are employed for the three significant electrocatalytic reactions such as oxygen reduction reaction (ORR), and methanol oxidation reaction (MOR), and hydrogen evolution reactions (HER). Thus, the novelty of the present work is not truncated with the adaption of facile synthetic procedure for co-doping but extends with exploring the multifunctional ability of the prepared electrocatalysts through adequate electrochemical studies.

2. Experimental methods and materials

2.1. Materials

The following high purity AR grade chemicals are used in the present study. Polyacrylonitrile (PAN), poly(methyl methacrylate) (PMMA), melamine ($C_3H_6N_6$), orthoboric acid (H_3BO_3), chloroplatinic acid (H_2PtCl_6), methanol (CH_3OH), Nafion ($C_7HF_{13}O_5S{\cdot}C_2F_4$), polyvinylidene fluoride or PVDF -$(C_2H_2F_2)_n$-with a molecular weight of 534,000, and N-methyl-2-pyrrolidone (NMP) were purchased from Sigma–Aldrich (USA). Dimethylformamide (DMF), formaldehyde (HCHO), ethylene glycol (EG), sodium hydroxide (NaOH), hydrochloric acid (HCl), sulphuric acid (H_2SO_4), absolute ethanol (CH_3CH_2OH), and isopropyl alcohol ($CH_3CHOHCH_3$) were purchased from Himedia Laboratories Pvt. Ltd. Carbon cloth is used as substrates to coat the active material. A high-purity stainless steel sheet is used as the current collector for electrochemical studies. Commercial Pt/C (20 wt% Pt on Vulcan XC72 Carbon; Pt particle size: 3–3.5 nm) is purchased from Sainergy Fuel Cell India Pvt. Ltd.

2.2. Preparation of B and N doped carbon nanofibers (HCNFs)

The electrospun carbon nanofibers were prepared by a simple electrospinning technique followed by the controlled pyrolysis of the resultant electrospun nanofibers. The typical preparation of CNF involves four steps that include ink preparation, electrospinning, stabilization, and pyrolysis. The precursor solution is prepared by dissolving the base polymers (PAN & PMMA) homogeneously with necessary precursors in the DMF solution under continuous stirring for 24 h at 80 °C. The resultant ink is loaded into a plastic syringe for the subsequent process of electrospinning. The applied voltage, needle-collector distance, and stream rate were optimized to be 15 kV, 15 cm, and 0.75 mL h^{-1}, respectively. The obtained electrospun nanofibers were initially stabilized in the air at 250 °C for 2 h. Followed by stabilization, the pyrolysis is carried out under a nitrogen atmosphere at 800 °C for 2 h with a heating rate of 2 °C min^{-1}. Melamine and orthoboric acid are used as N and B sources for doping. Based on the varied proportions of B and N sources, the CNF samples are named HCNF-I, II, III, IV, and V. The HCNF-I is devoid of orthoboric acid, whereas the HCNF-V is free from melamine. The three intermediate CNF samples, HCNF-II, III, and IV, are prepared out of the appropriate quantity of orthoboric acid and melamine in the ratio of 25:75, 50:50, and 75:25 respectively.

2.3. Preparation of Pt loaded carbon nanofibers

The dispersion of platinum nanoparticles on the prepared HCNF carbon supports is carried out by an impregnation and reduction process. The desired amount of HCNF is initially dispersed in double distilled water under ultrasonication for 30 min. Subsequently, 60 μL of chloroplatinic acid is diluted with 10 mL of deionized water under ultrasonication for 15 min, which was added slowly into the support solution and kept for 2 h under continuous stirring. Further, the pH of the resultant solution is adjusted to 14 by adding an appropriate amount of 1 M NaOH. Finally, 5 mL of conc. HCHO is used as a reducing agent and is added dropwise into the above mixture for a period of 1 h. The resultant homogeneous solution is refluxed for 3 h at 120 °C under a controlled atmosphere. After the completion of the reaction, an appropriate quantity of 1 M HCl is added to the cooled suspension to normalize the pH value to 7. The sample is then washed several times with water and ethanol and dried overnight in a vacuum at 80 °C to obtain the desired Pt/HCNF electrocatalysts.

2.4. Characterization of HCNFs and Pt/HCNFs

Rigaku D/Max 2400 X-ray diffractometer (Japan) with Cu Kα radiation (λ = 1.5418 Å) is used for X-ray diffraction. FESEM (Quanta 3D FEI, USA) and HRTEM (Hitachi HF-3300, Germany) are employed for morphological analysis. The FTIR spectrum was obtained using the FT-IR Bruker Tensor 27 spectrometer. The surface chemistry and valence states are examined using an X-ray photoelectron spectroscopy (SPECS FlexMod, Germany). The electrochemical workstation (Bio-Logic VMP3, France) is deployed for carrying out the electrochemical measurements.

2.5. Electrode preparation and electrochemical measurements

For the electrode preparation of ORR and MOR studies, the catalyst ink is prepared by mixing 4 mg of material with 100 μL of isopropyl alcohol, 300 μL of deionized water, and 8 μL of 5 wt% Nafion and sonicated for the complete dispersion of active material. Finally, 5 μL of the prepared ink is drop-casted on the glassy carbon electrode (diameter: 3 mm, area: 0.0706 cm^2). For HER, carbon cloth (1 × 1 cm^2) pre-treated with concentrated HCl is coated with active material along with carbon black and PVDF in a ratio of 80:10:10 using NMP (0.4 mL). The prepared cloth electrodes are dried at 80 °C in a vacuum for 12 h. In the present work, all the electrochemical measurements are carried out in an acidic electrolyte (0.5 M H_2SO_4 or 1 M H_2SO_4 + 1 M CH_3OH) using a standard three-electrode system. Pt coil and Ag/AgCl are used as counter and reference electrodes, respectively. In particular, the graphite rod is used as a counter electrode for the HER measurements. The applied potentials against Ag/AgCl are calibrated to a reversible hydrogen electrode (RHE). The electrochemical measurement of the benchmark electrocatalyst, 20 wt% Pt/C on Vulcan XC72 Carbon (Sainergy Fuel Cell India Pvt. Ltd.) is also carried out.

3. Results and discussion

3.1. Physicochemical properties of HCNFs

The evolution of structural defects by incorporating different proportions of B and N into the carbon milieu is evaluated quantitatively with Raman spectroscopy (Fig. 1a). Analysis of peak positions and intensities provides information about the changes in structural characteristics of CNFs, resulting from the boron and nitrogen doping. The prepared HCNFs exhibit two characteristic peaks at 1350 and 1590 cm^{-1} corresponding to the D- and G-bands. The D-band originates from the structural defects in the carbon lattice, while the G-band is generated due to the in-plane tangential stretching of sp^2 bonded graphitic carbon [12]. The intensity ratio of the D to the G band is calculated to determine the degree of graphitization or defect density of the prepared carbon nanostructures. The obtained values are 0.99, 1.01, 1.03, 1.13, and 1.16 for HCNF-I, II, III, IV, and V, respectively. A higher I_D/I_G ratio of 1.16 is obtained for HCNF-V, indicating that CNFs doped with B alone demonstrate a much more defective structure than the other HCNFs [4,13]. Even though the defect sites generated from dopants act as favorable anchoring spots for nanoparticle dispersion, the introduction of excessive defects can deteriorate the morphological features of CNFs [2].

The Fourier transform infrared spectra (Fig. 1b) show two clear bands around ~1569 and ~1390 cm^{-1} corresponding to the C═C, and C—N stretching vibrations, respectively [13,14]. Similarly, the B—N and B—C stretching vibrations are seen around 1290 and 1190 cm^{-1}, respectively [13,15]. The peak around 1095 cm^{-1} can be attributed to the C—O—C stretching vibrations [16]. Furthermore, the peaks around 1013, 776, and 695 cm^{-1} are ascribed to the asymmetric B—O stretching vibrations, *h*-BN out-of-plane bending, and B—OH bending vibrations, respectively [14,15]. Thus, the above result corroborates the successful boron and nitrogen doping in the carbon nanofibers with a significant C—N, B—C, and B—N bonding response.

X-ray photoelectron spectroscopy (XPS) measurements are carried out to validate further the co-doping of boron and nitrogen in the prepared carbon nanofibers. The presence of C 1s, O 1s, N 1s, and B 1s peaks at 285.2, 533.1, 399.9, and 190.8 eV, respectively, in the survey spectra of HCNFs (Fig. 2a) ensures the existence of heteroatoms and oxygen functionalities in the carbon milieu [17]. As per the preparation conditions, the HCNF-I is free from B doping and is substantiated by the absence of B 1s spectral features in the survey spectrum. On the other hand, even though HCNF-V is free from N, a remarkable measure of nitrogen is observed due to nitrogen-rich PAN as the base polymer and N_2 as the carbonizing environment. Fig. 2b shows the deconvoluted N 1s core-level spectra into three peaks at 397.8, 398.6, and 400.8 eV corresponding to the pyridinic, pyrrolic, and quaternary nitrogen functional groups, respectively [14]. Similarly, the deconvoluted B 1s core-level spectra (Fig. 2c) at 191.8 and 192.5 eV are attributed to the B—O bonds of BC_2O and BCO_2, respectively [18,19]. However, the oxidation of boron atoms is in agreement with the previous reports [20]. The peak at 190.7 corresponding to B-N is insignificant in HCNF-II & III. It gets intensified with HCNF-IV and V. The B-N bond inferring the bonded form of B and N dopants, which is detrimental for catalytic reactions owing to its inefficiency in breaking the inertness of carbon structures. It is also reported that the formation of B-N bonds is unavoidable during the simultaneous doping of boron and nitrogen in one step experimental procedure [18]. Table 1 shows the elemental composition of constituent elements in the prepared HCNFs obtained from the XPS analysis. As one could observe, HCNF-III possesses enhanced content of N with an optimal atomic weight percentage of B and O whereas, with HCNF-III and IV, the at. wt.% of oxygen increases tremendously with increasing content of B dopants. The calculated values of C/N, C/B, and N/B weight ratios of prepared HCNFs are given in Table 1. The HCNF-III has 66.8 at wt.% of carbon content with an optimal measure of B, N, and O functionalities compared to the other HCNFs. Thus, the XPS results provide adequate evidence for the co-doping of heteroatoms in the prepared carbon nanofibers.

The morphological evolution of the boron and nitrogen incorporated CNF is observed using FESEM micrographs (Fig. 3). The FESEM image of HCNF-I (Fig. 3a) shows the CNFs are tangle upon each other to form an average diameter of 156 nm (Fig. 3b). The HCNF-II and HCNF-III portray the formation of bundled structures that weave around 4–5 individuals resulting in an increased average diameter of 246 nm and 248 nm, respectively (Fig. 3c–f). The introduction of more defects in the co-doping of B & N has resulted in twisty carbon structures [2,21]. But, HCNF-IV carries a different morphological feature that unveils single strands CNFs (Fig. 3g) with an average diameter of 240 nm (Fig. 3h). Lastly, the HCNF-V displays ruptured CNFs with lateral lesions due to the excessive concentration of orthoboric acid that promotes the oxidation of CNFs [22]. Moreover, the average diameter of HCNF-V is a maximum value of 400 nm (Fig. 3(i,j)). Fig. S1a shows the FESEM image of HCNF-III for which the elemental mapping is performed. The uniform distribution of constituent elements such as C, O, N, and B is mapped with green, cyan, red, and orange spots in Fig. S1b. The individual mapping of each element has been provided in Fig. S1c–f, respectively. Thus, the representative elemental mapping of HCNF-III visibly ensures the uniform co-doping of B and N heteroatoms in the carbon milieu of prepared CNFs (Fig. S1).

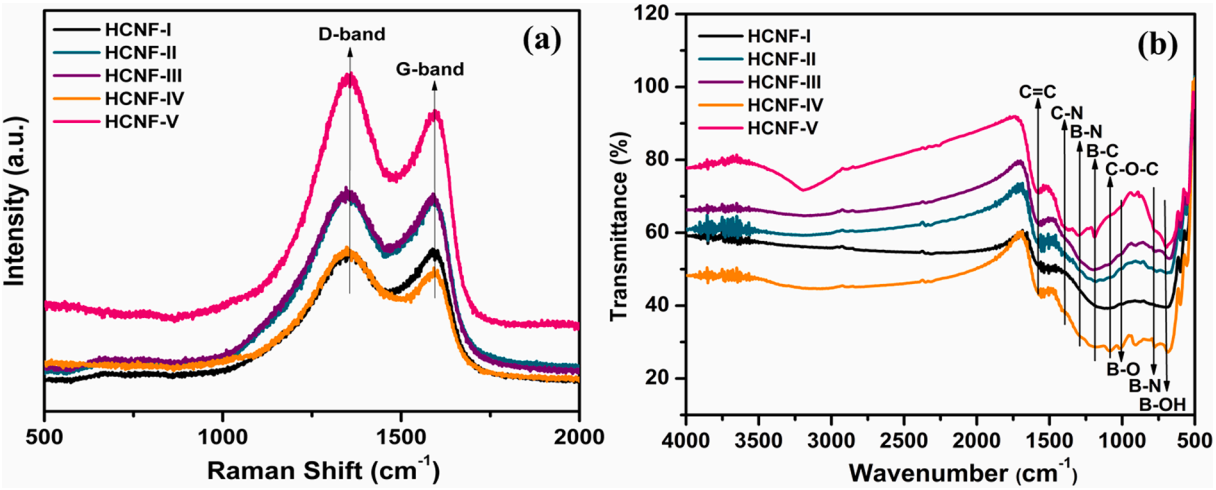

Fig. 1. (a) Raman spectra and (b) FT-IR spectra of HCNFs.

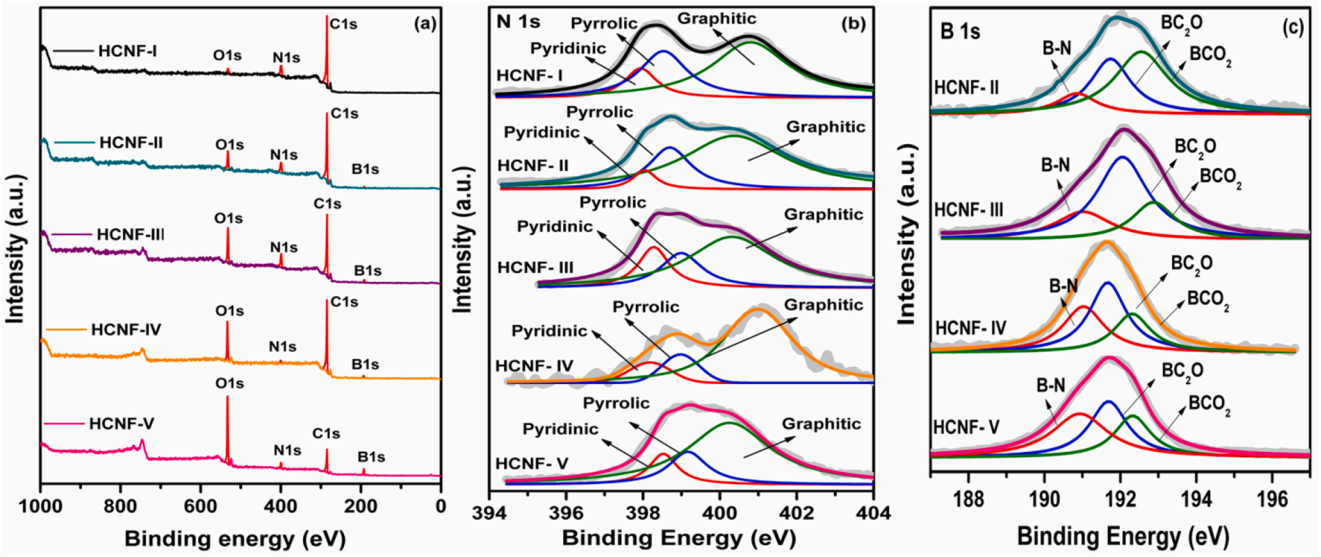

Fig. 2. XPS spectra: (a) survey spectra, (b) N 1s core-level spectra, and (c) B1s core-level spectra of HCNFs.

Table 1
The elemental composition of prepared HCNFs obtained from XPS analysis.

BN/CNFs	C (At. wt %)	O (At. wt %)	B (At. wt %)	N (At. wt %)	C/N	C/B	C/O	N/B
BN/CNF-I	86.1	3.1	–	10.7	8.05	–	27.77	–
BN/CNF-II	75.2	10.1	4.0	10.6	7.09	18.8	7.45	2.65
BN/CNF-III	66.8	14.6	6.2	12.3	5.43	10.77	4.58	1.98
BN/CNF-IV	62.2	20.1	9.3	8.4	7.40	6.69	3.09	0.90
BN/CNF-V	34.0	39.4	20.4	6.3	5.40	1.67	0.86	0.31

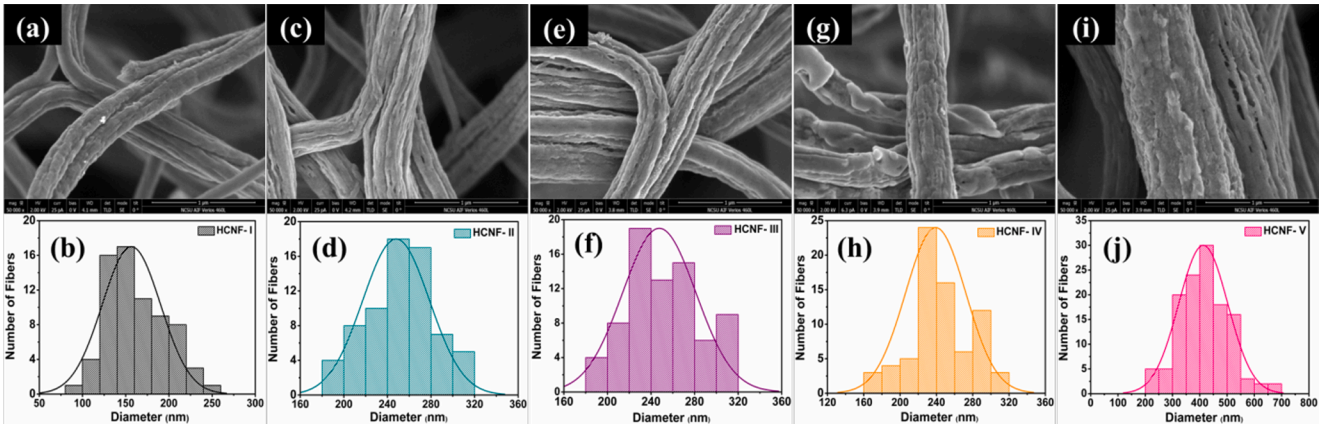

Fig. 3. FESEM micrographs and size distribution histograms of (a,b) HCNF-I, (c,d) HCNF-II, (e,f) HCNF-III, (g,h) HCNF-IV, and (i,j) HCNF-V.

3.2. Physicochemical properties of Pt/HCNFs

A facile polyol-assisted formaldehyde reduction protocol has loaded all the prepared HCNFs with Pt nanoparticles (Pt NPs). Fig. 4(a–o) shows the TEM micrographs of Pt/HCNFs and their corresponding particle size histograms. The Pt NPs are dispersed homogeneously without any agglomeration. Moreover, the loading of Pt NPs does not alter the initial morphology of the prepared CNFs. The particle size of Pt nanoparticles is measured using the Scion Image software for obtaining the size distribution histogram. The average particle size is around 2.4, 2.2, 1.8, 2.3, and 2.9 nm for Pt/HCNF-I, Pt/HCNF-II, Pt/HCNF-III, Pt/HCNF-IV, and Pt/HCNF-V, respectively. Based on the average particle size of Pt NPs, the geometrical surface area (GSA) calculated using Eq. (1), where ρ is the density of Pt metal (≈21.4 g cm^{-3}), and *d* is the average diameter of Pt NPs (nm). The obtained values are 116.39 m^2 g^{-1} for Pt/HCNF-I, 126.75 m^2 g^{-1} for Pt/HCNF-II, 156.72 m^2 g^{-1} for Pt/HCNF-III, 124.94 m^2 g^{-1} for Pt/HCNF-IV, and 94.09 m^2 g^{-1} for Pt/HCNF-V. Thus, among the prepared Pt/HCNFs, the Pt/HCNF-III possesses a higher geometrical surface area because of its smaller average particle size and narrow size distribution [23].

$$GSA\left(m^2 g^{-1}\right) = \frac{6}{\rho \times d} \quad (1)$$

Fig. 5 shows the representative physicochemical studies of Pt/HCNF-III. Fig. 5a,b depicts the HRTEM image of Pt/HCNF-III that defines the crystalline nature of the dispersed Pt NPs with well-defined lattice fringes. The measured interplanar spacing is around 0.22 nm, corresponding to the (1 1 1) planes of the Pt NPs. The SAED pattern of Pt/

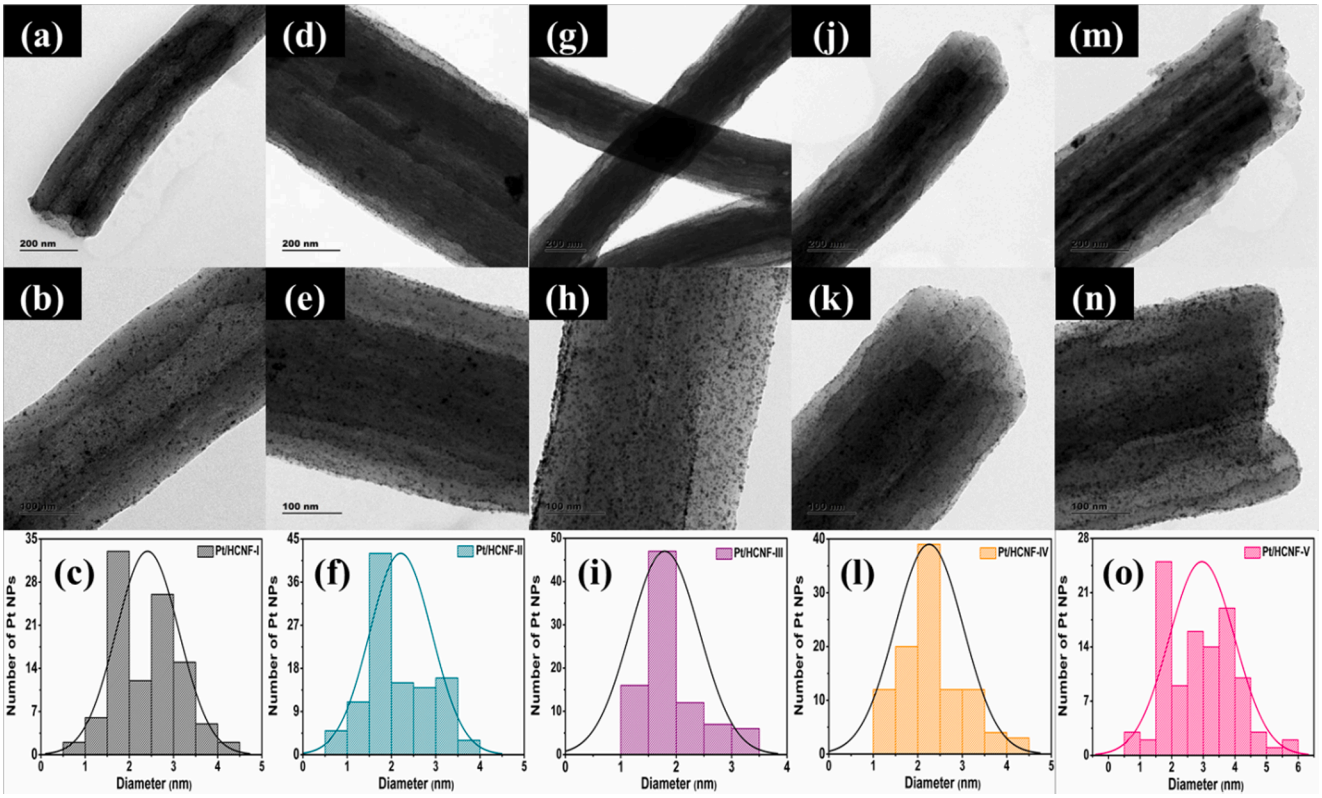

Fig. 4. TEM micrographs and corresponding particle size histograms of Pt/HCNFs: (a–c) P Pt/HCNF-I, (d–f) Pt/HCNF-II, (g–i) Pt/HCNF-III, (j–l) Pt/HCNF-IV, and (m–o) Pt/HCNF-V.

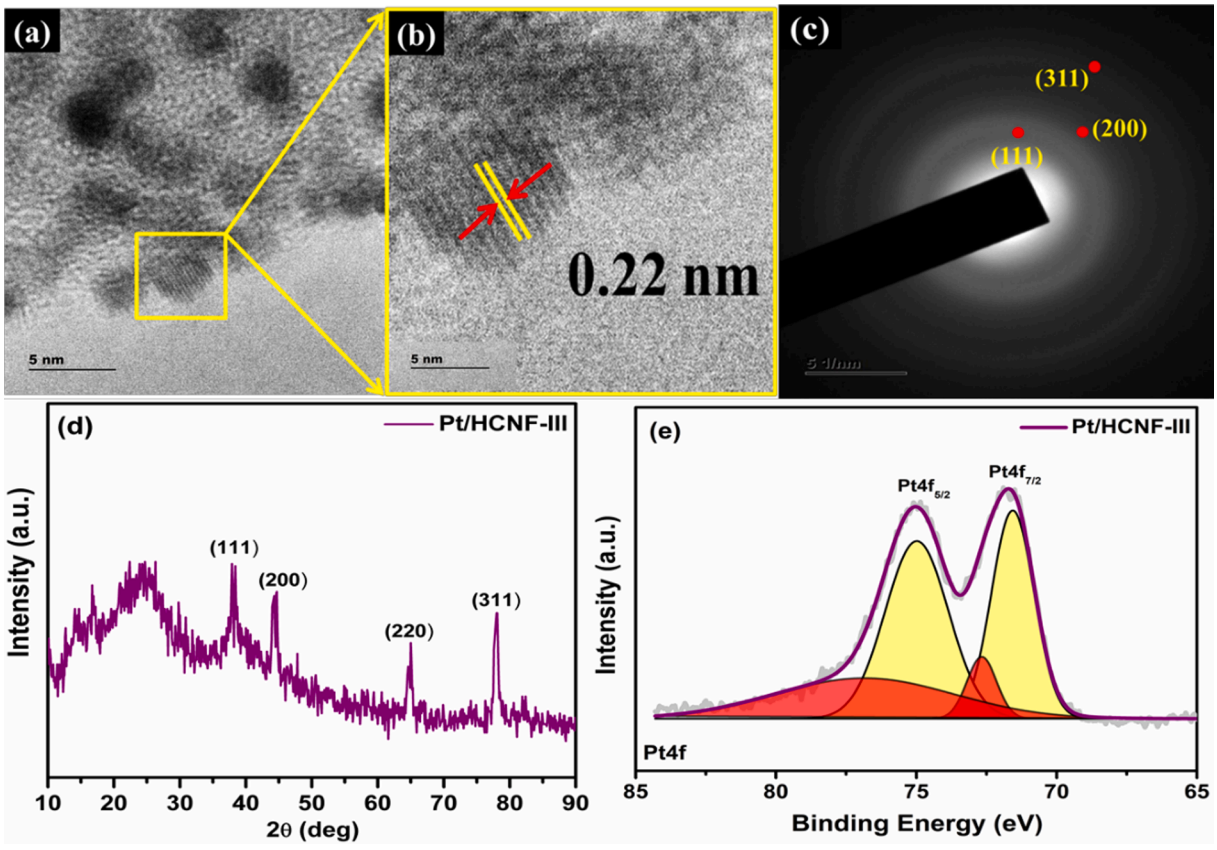

Fig. 5. (a) HRTEM image, (b) enlarged view of HRTEM image with lattice fringes, (c) SAED pattern, (d) XRD pattern, and (e) Pt4f high-resolution core-level spectrum of Pt/HCNF-III.

HCNF-III (Fig. 5c) portrays the circular fringes corresponding to the (1 1 1), (2 0 0), and (3 1 1) planes matching well with the JCPDS card no. 70-2431. The XRD pattern of Pt/HCNF-III (Fig. 5d) reveals that the loading of platinum over carbon nanofibers by obtaining the diffraction peaks at 39.75°, 46.23°, 67.45°, and 81.24° for Pt (JCPDS card no. 70-2431) along with the broad peak of carbon around 25°. The XPS analysis is carried out to investigate the chemical valence state of dispersed Pt in the Pt/HCNF-III sample. The obtained Pt 4f core-level spectrum (Fig. 5e) shows the Pt $4f_{5/2}$ and Pt $4f_{7/2}$ spin-orbital splitting deconvoluted into two pairs of peaks corresponding to Pt^0 (75.06 and 71.71 eV) and Pt^{2+} (75.78 and 72.39 eV) oxidation states, respectively. Pt^0 takes up a significant contribution confirming the deposition of metallic Pt, which is beneficial for electrocatalytic performance [24]. Moreover, the observed doublets shifted more positively than the typical Pt 4f spectrum indicating the strong interaction between the Pt NPs and the HCNF-III support, which is favorable for the electrocatalytic activity and stability of the prepared Pt/HCNF-III [25,26]. The core-level spectra for C, N, and B in the Pt/HCNF-III are given in Figure S2. The peaks at 284.61, 286.24, and 288.31 eV in C1s are ascribed to the sp2, C—N, and C═O, respectively. Similarly, the deconvoluted N1s spectra infer the presence of pyridinic and pyrrolic type carbon by observing the binding energies at 398.7 and 400.5 eV [27,28]. It is worth noticing that no prominent peaks were aroused in the B1s spectra. This might be due to the outer surface attachment of the B atom on the CNF and the relatively lower concentration than carbon (B/C) [29].

4. Electrocatalytic properties of Pt/HCNFs

4.1. Electrochemical impedance analysis

The electrochemical impedance analysis (EIS) is initially carried out for all the prepared Pt/HCNFs electrodes to evaluate the intrinsic charge transfer resistance and solution resistance at the electrode-electrolyte interface. A single arc in the high-frequency region followed by a nearly vertical straight line to the real impedance axis in the low-frequency region for all Pt/HCNFs [Fig. S3]. The calculated charge transfer resistance, R_{ct} and R_s are 0.189, 0.114, 0.089, 0.192, & 0.307 Ω and 0.620, 0.618, 0.609, 0.743, & 0.818 Ω for Pt/HCNFs-I, II, III, IV, and V, respectively. The 45° slope of the straight line to the real impedance axis implies the Warburg resistance, R_w, infers the frequency-dependent ion-diffusion at the electrolytic inference of the electrode. Overall, the Pt/HCNF-III possessess minimal R_s (0.609 Ω), R_{ct} (0.089 Ω), and the shorter and vertical straight line at the low-frequency region. The results further substantiate the lower ion-diffusion resistance and enhanced reversible electrosorption of electrolytic ions on the electrode surface [30]. Since the electrode materials with good electronic conductivity and easy accessibility of ions afford enhanced electrochemical performance. Therefore, the Pt/HCNF-III is envisaged to deliver catalytic better activity than the other prepared Pt/HCNFs.

4.2. Oxygen reduction reaction

The oxygen reduction reaction studies of prepared Pt/HCNFs are carried out in 0.5 M H_2SO_4 using a rotating disk electrode. The linear sweep voltammograms were recorded at various rpm ranging between 300 and 1600 within a potential window of 1–0.3 V vs. RHE (Fig. S4(a-e)). The corresponding *Koutecky*-Levich (K-L) plots using Eq. (2) are shown in (Fig. S4(f-j)).

$$\frac{1}{J}=\frac{1}{J_L}+\frac{1}{J_K}=\frac{1}{B\omega^{\frac{1}{2}}}+\frac{1}{J_K} \tag{2}$$

$$B=0.62nFC_o(D_o)^{2/3}\vartheta^{-1/6} \tag{3}$$

where J_L and J_K represent the limiting current density and kinetic current density, respectively. The slope value, B (Eq. (3)), obtained from the K-L plot, is used to calculate the number of electrons transferred (n) during the oxygen reduction. Here, F is the Faraday constant ($F = 96485$ C mol^{-1}), C_0 (1.13×10^{-3} mol cm^{-3}), and D_o (1.9×10^{-5} cm^2 s^{-1}) is the bulk concentration and diffusion coefficient of O_2, and ν is the kinematic viscosity (9.5×10^{-3} cm^2 s^{-1}) of dissolved oxygen in 0.5 M H_2SO_4 electrolyte. The linear and non-intersecting K-L plots confirm the first-order kinetics of prepared Pt/HCNFs during ORR [31]. Moreover, the calculated number of electron transfers during ORR using K-L analysis is ~4. The LSV polarization curves of Pt/HCNFs and commercial Pt/C recorded at a particular rpm of 1600 are plotted discretely in Fig. 6a to compare the ORR catalytic activity. From the three distinct regions of the polarization curves, namely, the kinetic, mixed kinetic, and diffusion limiting regions, the relative parameters such as the onset potential, half-wave potential, and the limiting current density are obtained. Among these, Pt/HCNF-III exhibits positive onset and half-wave potentials of 0.90 V and 0.76 V vs. RHE, respectively. Similarly, the limiting current density is higher (3.14 mA cm^{-2}) than the other electrocatalysts and commercial Pt/C (2.35 mA cm^{-2}). Further, the mass activity of Pt/HCNFs is calculated using Eq. (4) [32].

$$M_A\left(Ag^{-1}\right)=\frac{J_K}{M_{Pt}} \tag{4}$$

At an applied potential of 0.85 V vs. RHE, the obtained mass activity of Pt/HCNFs are 9.19, 9.31, 10.23, 4.92, and 2.89 A g^{-1} for Pt/HCNF-I, II, III, IV, and V, respectively, where the Pt/HCNF-III possesses a maximum mass activity (10.23 A g^{-1}) than the other prepared electrocatalysts.

Fig. 6b shows the polarization curves of Pt/HCNFs obtained using a rotating ring disk electrode (RRDE). As shown in Fig. 6b, the RRDE records current simultaneously at both its disk and ring during ORR; the disk current ((I_D) corresponds to the current measured during reduction, whereas the ring current ((I_R) attributed to the undesirable production of H_2O_2 intermediates. The recorded ring currents in the range of microamperes, thus corroborating the mere production of detrimental intermediate and efficient reduction of O_2 at the catalytic sites. However, the single-dopant supported electrocatalysts Pt/HCNF-I and Pt/HCNF-V yield relatively maximum ring current than their co-doped counterparts. Besides, among the intermediate catalysts, the Pt/HCNF-III with an equal amount of B and N generates an extraordinarily minimal and consistent measure of ring current throughout the potential window. Since the RRDE provides quantitative evidence on H_2O_2 production in terms of the ring current, the electron transfer number calculated from RRDE is significantly incumbent for determining the reaction pathway of ORR. Therefore, the electron transfer number and % of H_2O_2 production are obtained (Fig. 6c) using Eqs. (5) and (6) [33].

$$n=4\frac{I_D}{I_D+\frac{I_R}{N}} \tag{5}$$

$$H_2O_2\%=\frac{200\frac{I_R}{N}}{I_D+\frac{I_R}{N}} \tag{6}$$

It shows that the calculated electron transfer number is around 4, and the corresponding % of H_2O_2 is less than 2 %. Hence, the Pt/HCNFs are perceived to follow an efficient four-electron pathway during ORR. The ORR on Pt catalytic sites is alleged to follow two different mechanisms like associative and dissociative at high and low current densities. During the dissociative reaction (Eqs. (7)–(9)), the ORR takes place as follows [34].

$$\frac{1}{2}O_2+Pt/HCNF\rightarrow Pt/HCNFO^* \tag{7}$$

$$Pt/HCNFO^*+H^++e^-\rightarrow Pt/HCNF-OH^* \tag{8}$$

$$Pt/HCNF-OH^*+H^++e^-\rightarrow H_2O+Pt/HCNF \tag{9}$$

Whereas, in the high current density region, the associative

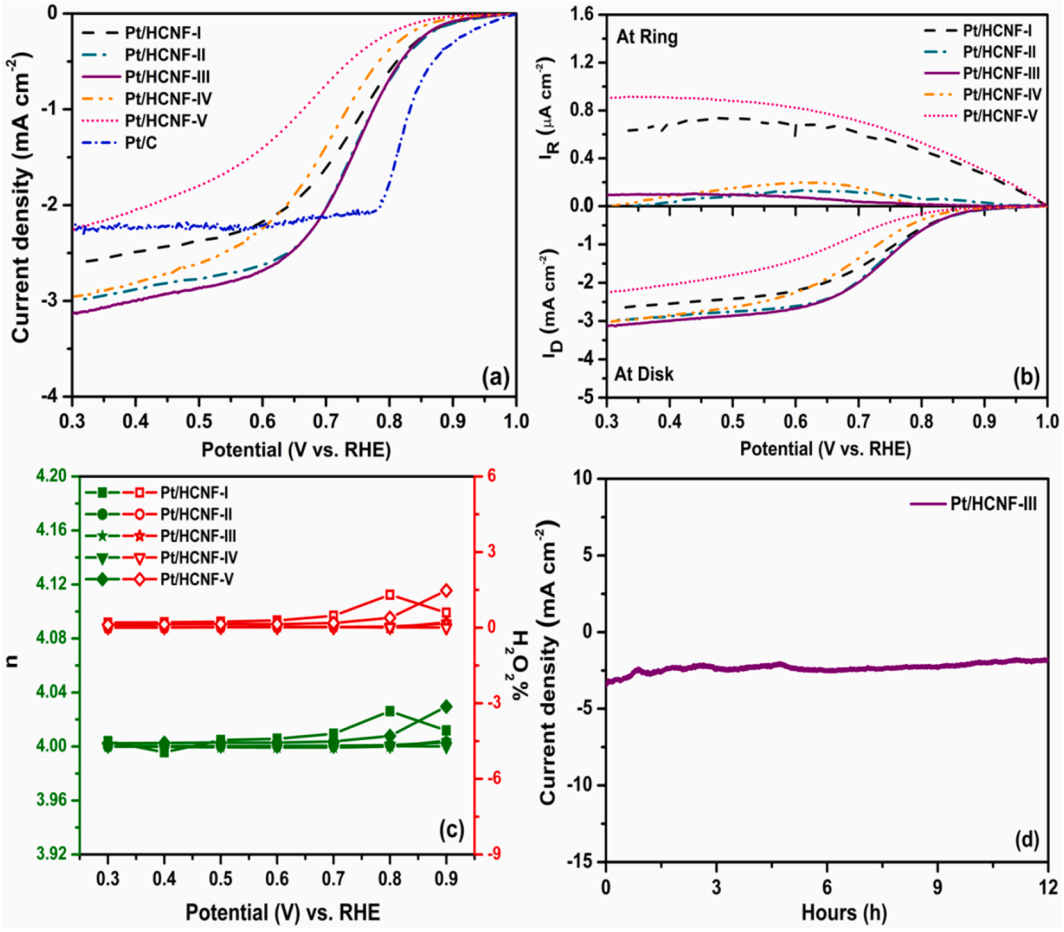

Fig. 6. (a) Comparative RDE polarization curves at 1600 RPM, (b) RRDE polarization curves at ring and disk, (c) calculated n and H_2O_2% of Pt/HCNFs, and (d) chronoamperometry of Pt/HCNF-III.

mechanism (Eqs. (10)–(14)) occurs as given below,

$$O_2 + 2Pt/HCNF \rightarrow Pt/HCNF_2O_2^* \quad (10)$$

$$Pt/HCNF_2O_2^* + H^+ + e^- \rightarrow Pt/HCNF_2 - O_2H^* \quad (11)$$

$$Pt/HCNF_2 - O_2H^* \rightarrow Pt/HCNF - OH^* + Pt/HCNF - O^* \quad (12)$$

$$Pt/HCNF - OH^* + Pt/HCNF - O^* + H^+ + e^- \rightarrow Pt/HCNF - OH^* + Pt/HCNF - OH^* \quad (13)$$

$$Pt/HCNF - OH^* + Pt/HCNF - OH^* + H^+ + e^- \rightarrow 2H_2O + 2Pt/HCNF \quad (14)$$

Thus, the prepared Pt/HCNFs are envisaged to follow the above reaction mechanism to reduce oxygen via a four-electron pathway.

Finally, the durability of Pt/HCNF-III towards ORR is evaluated using the chronoamperometry technique at an applied potential of 0.3 V vs. RHE for about 12 h under a continuous supply of oxygen (Fig. 6d). Even after 12 h of continuous and spontaneous reduction of oxygen, the negligible fall in current density validates the remarkable stability of prepared Pt/HCNF-III towards ORR. However, the ORR catalytic activity of Pt/HCNF-II, III, and IV, is much more significant than the Pt/HCNF-I and V. This is because the role of nitrogen and boron is discrete and remarkable in their way. Thus their synergistic presence in co-doped Pt/HCNFs enriches the catalytic activity of the CNF supports. Explicitly, the doping of nitrogen surges the conductivity of CNF support by increasing the charge density of the material and disturbs the arrangement of electrons, favouring the adsorption and reduction of O_2 molecules during ORR. As well as, the carbon atom imparts a positive charge on the comparatively less electronegative neighbouring B dopant, facilitating the chemisorption of negatively charged O_2 molecules and enhancing the ORR kinetics. Similarly, the B atoms as well render electrons during ORR since the P_z orbital of B can be received with the π-electron system of the CNF support [35]. Moreover, among the co-doped Pt/HCNFs, Pt/HCNF-III displays better activity due to the relatively high dispersal of Pt NPs with smaller particle sizes and agglomeration-free narrow size distribution. Table 2 shows the comparative ORR performance of prepared Pt/HCNFs with other related Pt-based electrocatalysts loaded on different carbon supports [36–43].

4.3. Methanol oxidation reaction

The cyclic voltammogram is obtained (Fig. 7a) to calculate the electrochemical active surface area (ECSA) of Pt/HCNF and commercial 20 wt% Pt/C in 0.5 M H_2SO_4. All the Pt/HCNFs and Pt/C exhibit the hydrogen adsorption and desorption peaks from which the ECSA (Fig. 7c) is calculated using Eq. (15).

$$ECSA\left(m^2 g^{-1}\right) = \frac{Q_H}{0.21 \times M_{Pt}} \quad (15)$$

where Q_H is obtained by taking a mean charge value from the integrated hydrogen adsorption and desorption regions, besides, 0.21 is the charge required to oxide the adsorbed hydrogen monolayer on a Pt surface, and M_{Pt} (30 μg cm^{-2}) is the mass loading of Pt on the surface of the glassy carbon electrode [39]. The calculated ECSA is 22.20, 47.98, 62.57, 25.94, and 16.56 m^2 g^{-1} for Pt/HCNF-I, II, III, IV, and V, respectively.

Table 2
The ORR performance of prepared Pt/HCNFs compared with other related recent reports.

ORR Electrocatalysts	Onset potential (V vs. RHE)	Half-wave potential (V vs. RHE)	Mass activity (A g^{-1}) At 0.9 V	Ref
Pt/BNGS	1.05	0.90	213.6	[1]
Pt/BNCNF	1.06	0.91	355.4	
Pt/CXG-130	0.94	0.78	NA	[36]
Pt/CXG-300	0.97	0.83		
Pt/N-CXG-130	0.97	0.82		
Pt/N-CXG-300	0.97	0.84		
Pt/NMC-1	NA	0.702	NA	[37]
Pt/NMC-2		0.658		
Pt/HD-CAs	1.07	0.89	NA	[38]
Pt/LD-CAs	0.86	0.71	NA	
Pt/RuO_2@ACT	0.923	0.805 V	NA	[39]
PtNW/S-CNT	NA	NA	272	[40]
PtNW/FCNT			204	
Pt/BZ	NA	NA	5.8	[41]
Pt/TOAS			4.9	
Pt/NBF-ReS_2/Mo_2CT_x	NA	0.911	63.3 mA/μg	[42]
Pt-Er@PC-900	1.092	0.93	29.79	[43]
Pt/HCNF-I	0.89	0.73	9.31	This Work
Pt/HCNF-II	0.89	0.75	9.19	
Pt/HCNF-III	0.90	0.76	10.23	
Pt/HCNF-IV	0.87	0.69	4.92	
Pt/HCNF-V	0.84	0.62	2.89	

Significantly, Pt/HCNF-III provides a higher ECSA than 20 wt% commercial Pt/C (49.61 m^2 g^{-1}). Generally, the ECSA of Pt-based electrocatalysts is higher due to the enhanced adsorption of electrolytic ions and protons. This enhanced adsorption is originated from the reinforcement of π-bonding and improved wettability at the electrode-electrolytic interface related to the dopant species [1]. From the ECSA, the platinum utilization percentage is calculated using Eq. (16) [23].

$$\text{Pt Utilization}\% = \frac{ECSA}{GSA} \times 100 \tag{16}$$

The utilization % of Pt/HCNFs-I, II, III, IV, & V is 19%, 37%, 40%, 21%, and 17%, respectively. Pt/HCNF-III exhibits a maximum Pt utilization percentage than the B or N dopant supported electrocatalysts. Thus, the Pt catalytic sites of Pt/HCNF-III are highly accessible to the electrolytic ions and connected to the carbon support's electronic conduction network.

Fig. 7b shows the cyclic voltammograms of the electrocatalysts measured in 0.5 M H_2SO_4 + 1 M CH_3OH electrolyte. It shows two anodic peaks around a potential of 0.65 V and 0.35 V vs. Ag/AgCl, respectively. The forward peak (I_f) around 0.65 V vs. Ag/AgCl gains profound significance since it represents methanol oxidation. In contrast, the reverse anodic peak (I_b) around 0.35 V vs. Ag/AgCl accounts for the oxidation of intermediate species adsorbed during the methanol oxidation [44]. From the forward peak current densities, the mass activity of the MOR electrocatalysts is calculated [45,46] using Eq. (17) and are 162.84, 236.18, 324.77, 223.89, and 61.19 A g^{-1}, respectively. Fig. 7c shows the bar diagram of calculated ECSA & M_A values of prepared Pt/HCNFs and 20 wt% commercial Pt/C.

$$M_A\left(Ag^{-1}\right) = \frac{I_f}{M_{Pt}} \tag{17}$$

Among the prepared Pt/HCNFs, Pt/HCNF-III displays a relatively better forward peak current density and mass activity when compared with the commercial 20 wt% Pt/C. Hence, integrating the benefits of N and B, the Pt catalysts supported on co-doped CNF performs better than their singly doped counterparts during MOR. In particular, the N and B moieties facilitates uniform and agglomeration-free dispersal of Pt active catalytic sites in Pt/HCNF-III. Here, nitrogen doping plays a significant role in the generation of anchoring sites for the dispersal of Pt NPs. The boron doping increases the electron density and lowers the d-band centre of Pt, which enhances the methanol oxidation activity by decreasing the C-H bond energy and adsorption energy of CO adsorbates [46]. The reaction mechanism of methanol oxidation on Pt catalytic sites of Pt/HCNFs is supposed to follow a three-step process involving methanol dehydrogenation, the formation of CO_{ads} intermediates, and oxidative removal of CO_{ads} intermediates. Due to the dissociative chemisorption of methanol at the low polarisation region, yields Pt/HCNF-COH species (Eqs. 18–20). Here, the first dehydrogenation step is considered to be the rate-determining step.

$$Pt/HCNF + CH_3OH \rightarrow Pt/HCNF - CH_2OH^* + H^+ + e^- \tag{18}$$

$$Pt/HCNF - CH_2OH^* \rightarrow Pt/HCNF - CHOH^* + H^+ + e^- \tag{19}$$

$$Pt/HCNF - CHOH^* \rightarrow Pt/HCNF - COH^* + H^+ + e^- \tag{20}$$

In the high polarization region, the MOR kinetics is intricate due to the formation of poisoning CO_{ads} intermediates and oxygen-containing species. The CO_{ads} intermediates wrap the Pt catalytic sites and hinder the following reaction; hence the oxidative removal of CO_{ads} intermediates is considered the rate-determining step in the high overpotential region of methanol oxidation. The formation and removal of CO_{ads} at Pt/HCNFs take place, as mentioned in Eqs. (21) and (22) [46].

$$Pt/HCNF - COH^* \rightarrow Pt - CO + H^+ + e^- \tag{21}$$

$$Pt - CO + OH_{ads} \rightarrow Pt + CO_2 + H_2O \tag{22}$$

The I_f/I_b ratio is an essential parameter for identifying the anti-poisoning ability of the MOR electrocatalysts. Because the most undesirable existence of CO poisoning in the Pt-based electrocatalysts resulting the incomplete oxidation of methanol. The adsorption intermediate, Pt(CO_{ads}) generated during the forward scan get reduced to pure Pt at the backward scan; therefore, the ratio of forward peak current density to that of reverse peak renders the CO tolerance of the electrocatalysts [47]. The calculated I_f/I_b ratios are 2.16, 3.88, 2.58, 6.90, and 1.97 for Pt/HCNF-I, II, III, IV, and V, respectively. The prepared Pt/HCNFs render a relatively higher I_f/I_b ratio than 20 wt% commercial Pt/C (1.10). Thus, the Pt/HCNF-IV with a relatively maximal proportion of B concerning N provides a remarkable CO tolerance among the prepared electrocatalysts.

Further, the durability tests are carried out for all the Pt/HCNFs at an applied potential of 0.65 V vs. Ag/AgCl for a period of 2 h (Fig. 7d). The observed initial drop of current density is inevitable due to the coverage of residual intermediate species such as CO_{ads}, CH_3OH_{ads}, and CHO_{ads} on the catalytic Pt sites during the MOR [48]. The Pt/HCNF-IV with higher CO tolerance shows a relatively smaller drop in current density. Even though the Pt/HCNF-III renders relatively superior catalytic activity in terms of significant ECSA, forward peak current density, and mass activity, the CO tolerance of Pt/HCNF-IV is better concerning the high I_f/I_b ratio and enhanced stability. Since boron has a strong adsorption ability toward oxygen species, this might be due to the boosted ratio of boron dopants with respect to nitrogen. Boron exhibits a bifunctional mechanism of CO tolerance, which is prevalently known for PtRu/C electrocatalyst. The oxygen species adsorbed on boron could interact with and remove CO from the catalytic Pt sites and offer extraordinary CO tolerance. Thus, the bifunctional mechanism of boron dopants in Pt/HCNF-IV enhances the CO tolerance aptitude during methanol oxidation [49]. Table 3 shows the comparative MOR performance of prepared Pt/HCNFs with other related Pt-based electrocatalysts loaded on different carbon supports [50–57].

4.4. Hydrogen evolution reaction

The HER studies of Pt/HCNFs are carried out in 0.5 M H_2SO_4 at a

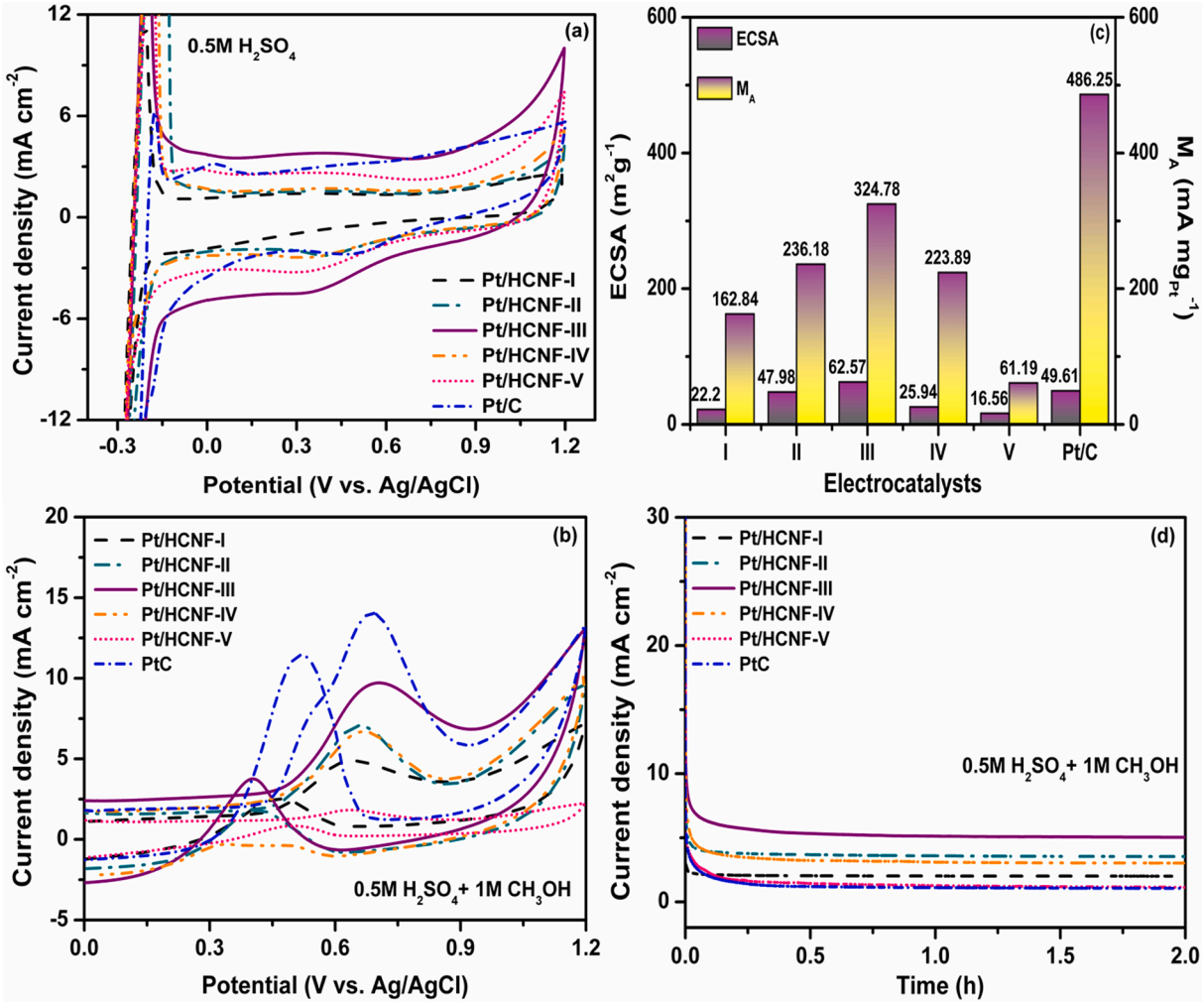

Fig. 7. (a) Cyclic voltammograms in 0.5 M H_2SO_4, (b) cyclic voltammograms in 0.5 M H_2SO_4 + 1 M CH_3OH, (c) bar diagram on calculated ECSA & M_A, and (d) chronoamperometry of Pt/HCNFs.

scan rate of 5 mV $s^{-1,}$ and the obtained polarization curves are given in Fig. 8a. The Pt/HCNF-III exhibits comparable catalytic activity with commercial Pt/C in terms of early-onset than the other prepared electrocatalysts. The onset potentials of the electrocatalysts follow the order of Pt/C (−0.0060 V) < Pt/HCNF-III (−0.0117 V) < Pt/HCNF-II (−0.0178 V) < Pt/HCNF-IV (−0.0238 V) < Pt/HCNF-I (−0.0267 V) < Pt/HCNF-V (−0.0326 V). The obtained overpotentials are given in Fig. 8b, where the Pt/HCNF-III demands a minimal overpotential of 54 mV than the other prepared Pt/HCNFs. Further, the mass activity (A g^{-1}) is calculated using Eq. (23) at an overpotential of 200 mV to understand the HER catalytic activity of the electrocatalysts [58].

$$M_A\left(Ag^{-1}\right) = \frac{I_{200mV}}{M_{Pt}} \tag{23}$$

The mass activity of Pt/HCNF-I, II, III, IV, and V are 2.314, 3.419, 6.166, 3.757, and 4.993A g^{-1}, respectively. Significantly, a higher mass activity of 6.166 A g^{-1} is attained by Pt/HCNF-III. Besides, the Tafel analysis determines the reaction pathway of Pt/HCNFs during HER, and the obtained Tafel plot is given in Fig. 8c. Concerning the reaction mechanisms of HER in an acidic medium, it is alleged to follow either of the two pathways, namely the Volmer–Heyrovsky or Volmer–Tafel pathways [59]. The obtained Tafel values envisage the rate-determining step and reaction pathway of the prepared Pt/HCNFs. During the first step of HER, the adsorbed hydronium ion (H_3O^+) at the catalytic surface of Pt/HCNFs gets an electron to form an adsorbed hydrogen atom (Pt/HCNF-H_{ads}), and this is referred to as Volmer or discharge reaction. The second step of HER can take either of two reactions: Heyrovsky/desorption reaction or Tafel/recombination reaction. During the Heyrovsky reaction, the hydrogen adsorbate gains an electron and a proton/H_3O^+ to form a hydrogen molecule that gets desorbed from the catalytic site and evolves as hydrogen gas. Instead, if the Tafel reaction occurs, two hydrogen adsorbates recombine at the electrode surface to evolve hydrogen. The HER reaction steps of Pt/HCNFs are deliberated below (Eqs. (24)–(26)).

$$Pt/HCNF - COH^{*} \rightarrow Pt - CO + H^{+} + e^{-} \tag{24}$$

$$Pt/HCNF - H_{ads} + H_3O^{+} + e^{-} \rightarrow H_2 + Pt/HCNF + H_2O \tag{25}$$

$$Pt/HCNF - H_{ads} + Pt/HCNF - H_{ads} \rightarrow H_2 + Pt/HCNF \tag{26}$$

The calculated Tafel slopes of Volmer-Heyrovsky-Tafel reaction steps are 120 mV/dec, 40 mV/dec, and 30 mV/dec, respectively. In the present work, the Tafel slopes of Pt/HCNF-I, II, III, IV, and V are 51, 38, 33, 39, and 62 mV dec^{-1}, respectively. The Pt electrocatalysts supported on co-doped CNFs, namely Pt/HCNF-II, III, and IV, demand a minimal Tafel slope value. Significantly, Pt/HCNF-III exhibits a Tafel slope of 33 mV dec^{-1} that is nearly identical to that of commercial Pt/C (31 mV dec^{-1}), and it follows the Volmer-Tafel pathway of hydrogen evolution. The rest of the Pt/HCNFs follow the Volmer-Heyrovsky route with desorption as a rate-determining step during HER. Since Pt/HCNF-III is observed to be a better catalyst than all the other prepared Pt/HCNFs in terms of early-onset, minimal overpotential, and Tafel slope, the durability test is

Table 3
The MOR performance of prepared Pt/HCNFs compared with other related recent reports.

MOR electrocatalysts	ECSA ($m^2 g^{-1}$)	I_f (mA cm^{-2})	I_b (mA cm^{-2})	I_f/I_b	Mass activity (A g^{-1})	Ref
Pt/3D-SPG	79.65	2.87	2.62	1.095	NA	[50]
Pt/SPG	68.97	1.75	1.63	1.073		
Pt/PG	60.88	1.30	1.21	1.074		
Pt/Co_2C-Mo_2C@CS	64.47	NA	NA	NA	1504.5	[51]
PEDOT/DLHCs/Pt	59.45	NA	NA	1.15	807	[52]
Pt NDs/Fe-N-S-GR	104.7	NA	NA	NA	932.7	[53]
Pt/Fe-N-GR	51.7				533.7	
Pt/GO	56.3				397.2	
Pt/N-MWCNTs	94.61	NA	NA	NA	539.4	[54]
Pt/AO-MWCNTs	78.88				450.3	
Pt/SC	55	NA	NA	1.18	201	[55]
Pt/GA	NA	8.72	4.32	2.02	NA	[56]
Pt/NGA		9.42	4.63	2.03		
Pt/BGA		19.28	18.31	1.05		
Pt/HGN-10 min-900	74.8	NA	NA	NA	377.5	[44]
Pt/HGN-1 h-900	72.7				254.6	
Pt/CRGO-900	33.1				206.1	
$Pt_{0.7}Ru_{0.25}Ir_{0.05}$	78.35	NA	NA	1.37	1721	[57]
Pt/HCNF-I	19.20	1.86	0.85	2.16	162.84	This Work
Pt/HCNF-II	47.98	7.09	1.83	3.88	236.18	
Pt/HCNF-III	58.57	9.74	3.75	2.58	324.77	
Pt/HCNF-IV	25.94	6.72	0.95	7.08	223.89	
Pt/HCNF-V	17.86	4.89	2.52	1.97	61.19	

carried out for Pt/HCNF-III and is provided in Fig. 8d. The chronoamperometry is taken at an applied potential of 0.050 V vs. Ag/AgCl for a period of 24 h. After an insignificant and gradual drop of current density during the initial hour of CA, the Pt/HCNF-III delivers a remarkable HER catalytic activity throughout the entire stability study.

The enhanced HER electrocatalytic performance of Pt/HCNF-III is highly attributable to the synergistic presence of boron and nitrogen in the CNF support because of the changes induced in the local charge density and asymmetry spin density of doped carbon support influences the HER performance [60]. N doping increases the active sites for the nucleation and growth of Pt NPs by inducing the defects and strain on the carbon support, enhances the conductivity by facilitating the electron transfer kinetics; and reduces the electrochemical energy barrier by polarizing the neighboring carbon atoms. The positively charged carbon atoms adjoining the N dopants act as active sites for hydrogen adsorption and facilitate the Volmer reaction, thereby reducing the energy barrier towards HER [61]. Similarly, the neighboring of B dopants with C atoms in co-doped HCNFs affect valence orbital energy levels of CNFs, thus reducing ΔGH* and facilitating HER. It has been reported that boron dopants are stable under 0.5 M H_2SO_4 aqueous solutions, which inhibits the detachment of Pt catalytic sites from CNFs during the long-term durability of HER. Moreover, the B dopants form a stable octet coordinate with lone pair electrons of an oxygen atom in the water molecule and enhance the wetting ability of prepared carbon support by providing easy release of protons [62]. Thus, the Pt/HCNF-III with an optimal boron and nitrogen moieties ratio delivers an enriched catalytic activity towards HER. Table 4 shows the comparative HER performance of prepared Pt/HCNFs with other related Pt-based electrocatalysts loaded on different carbon supports [63–72].

5. Discussion on DIMSI effect

The role of heteroatom (B/N) doping in the metal-support interaction and catalytic activity of prepared Pt/HCNFs is discussed below. In general, the loading of Pt NPs on the carbon support creates a local electrostatic potential perturbation at the interface, which infers the strength of the interaction between the metal surface and carbon support. However, the generation of perturbation is strictly associated with the electronic structure of both the metal and the support [73]. Following the metal–semiconductor boundary layer theory, when two phases get in contact, thermodynamic equilibrium is attained, provided the Fermi energy level of the electrons of the two entities is the same at the interface. This equalization of Fermi levels is possible with the flow of electrons across the interface, which depends on the relative work function of electrons in the metal and the support. This electron transfer sets up charge difference at the interface leading to the re-hybridization of electron orbitals. It creates changes in the d-band population and the density of states at the Fermi level. This serves as the basis of electronic type metal-support interaction [1]. Thus, incorporating B and N in the CNF milieu creates re-localization of electrons and generates variations in the local density of states that, in turn, increase or decrease the work function of the carbon support. This modification in the electronic structure of CNFs influences the metal-support interaction via the charge transfer and hybridization of electron states between the Pt NPs and CNFs.

On the other hand, the role of DIMSI on catalytic activity is discussed further. The first step of the electrocatalytic reaction is the adsorption of reactant molecules on the Pt catalytic sites. Subsequently, a chemical bond is established between the metal surface and the adsorbate molecule on account of adsorption. Following the d-band theory, the interaction between the valence states of adsorbate and s and d states of the Pt NPs give rise to the bond formation. Initially, the renormalization of adsorbate occurs from the interaction of valence states of adsorbate and the s states of metal. Further, the renormalized adsorbate interacts with the d states and results in the generation of discrete bonding and anti-bonding states. Moreover, the relative filling of these states infers the strength of bonding between the adsorbate and metal surface, whereas the filling of anti-bonding states weakens the bond strength. However, the higher energy of anti-bonding states with respect to the Fermi energy lowers the filling degree and strengthens the bond. Furthermore, the centre of the d-band is considered for the relative comparison with Fermi energy and evaluation of bond strength. The heteroatom doped CNF support thus varies the position of platinum's d-band and affects the adsorbate bonding and influences the catalytic activity of electrocatalysts via dopant-induced metal-support interaction (DIMSI). The benefits of DIMSI are due to the role of distinct electronic effects such as the matching of electronic structures of CNFs and that of loaded Pt NPs, the totality of bonds formed between the Pt NPs and C, N, & B surface atoms, breakdown of long-range electronic de-localization, local surface deformation by the intervention of surface defects, and re-distribution of electron density. Moreover, the consequences of DIMSI towards the catalytic activity can be attributed to the alteration of adsorption properties owing to the changes in the electronic structure and improved metal particle dispersion [1].

To conclude, the Pt electrocatalysts loaded on boron and nitrogen co-doped CNF supports accomplish better catalytic activity than their single dopant counterparts and this might be due to the following reasons, (i) the most appropriate choice of dopants for carbon, B and N with the electronegativity order of (B < C < N) ensures successful co-doping, (ii) N doping imparts positive charge on neighbouring C sites and benefits oxygen adsorption while the positively charged B sites resulting from the conjugation of boron dopants with π system of carbon facilitates O_2 reduction, (iii) modification of surface structure and electronic properties aids the nucleation and dispersion of Pt electrocatalysts on CNFs, (iv) the co-doping also enhances the stabilization of Pt NPs on carbon support via dopant induced metal support interaction mechanism, and hinders the agglomeration of Pt NPs, (v) the electron transfer properties of carbon support is significantly enhanced, (vi) the generation of defects also act as anchoring sites for dispersion of platinum, (vi) the

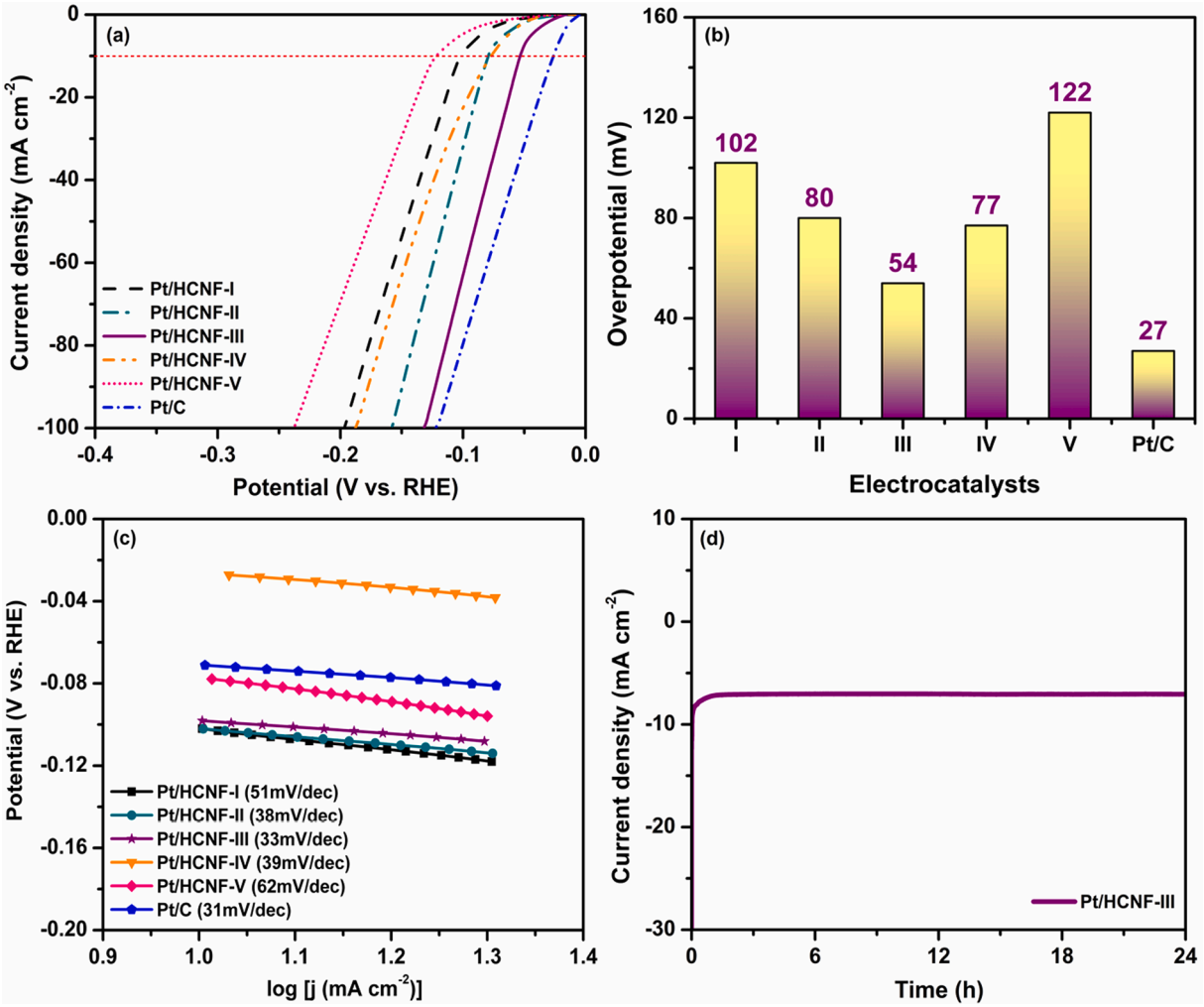

Fig. 8. (a) HER polarization curves, (b) bar diagram on overpotential at 10 mA cm^{-2}, and (c) Tafel plot of Pt/HCNFs, and (d) chronoamperometry of Pt/HCNF-III.

improved wettability of doped carbon supports increases the interactions with the electrolytic solution, (vii) the local chemical reactivity of carbon support is modified and thus enhances the binding energy of Pt atoms, and (viii) the adsorption of Pt NPs on CNFs is mediated via two different mechanisms; nitrogen activates the neighbouring C site for Pt adsorption, whereas boron involves in direct chemical bonding with Pt. Furthermore, among the other co-doped supports, HCNF-III with optimal doping of boron and nitrogen moieties displays a sensible I_D/I_G ratio. The ideal defective structure of HCNF-III ensures significant anchoring sites for the nucleation of Pt NPs and facilitates uniform loading of platinum with narrow size distribution and smaller average particle size. Besides, the agglomeration of Pt NPs is also wholly controlled in Pt/HCNF-III. Hence, Pt/HCNF-III exhibits maximum ECSA and Pt utilization ratio, resulting in enhanced electrocatalytic activity towards ORR, MOR, and HER.

6. Conclusion

Successful co-doping of CNFs with boron and nitrogen heteroatoms is accomplished using a facile single-step electrospinning technique. The evidential presence of B & N related functional moieties from the spectroscopic investigations corroborates boron, and nitrogen doping in the prepared CNF supports. The presence of undesirable B-N bonds is insignificant with an optimal measure of dopants in HCNF-II & III and gets intensified with HCNF-IV&V. The Raman analysis depicts the relatively defective structure of HCNF-V than the other prepared HCNFs. The evolution of morphological characteristics on single doping of B or N and varied proportions of B & N co-doping is also investigated. The morphological features of HCNF-IV & V get destructed owing to the proportional increase of oxygen functionalities and boron dopants, leading to excess oxidation of CNFs. The elemental mapping further validates the uniform doping of both boron and nitrogen in the carbon milieu of prepared HCNF-III. Besides, the effect of the varied proportion of B & N doping on Pt dispersion is investigated for the optimization of better Pt catalyst support. The TEM analysis of Pt/HCNFs exhibits the uniform and narrow size distribution of Pt NPs with smaller average particle size and agglomeration-free dispersion on the Pt/HCNF-III electrocatalyst. The prepared Pt/HCNF-III renders better electrocatalytic activity towards ORR following an efficient 4-electron pathway involving a negligible measure of undesired hydrogen peroxide intermediate. Moreover, Pt/HCNF-III provides significant ECSA (62.57 m^2 g^{-1}) higher than commercial Pt/C (49.61m^2 g^{-1}) and sensible Pt utilization ratio (40%) than other Pt/HCNFs. Pt/HCNF-III displays a relatively higher mass activity of 324.77 and 6.17 A g^{-1} during MOR and HER, respectively. Pt/HCNF-III also demands a minimal overpotential (54 mV) and Tafel slope (33 mV dec^{-1}) during HER. Moreover, Pt/HCNF-III also has enhanced durability with negligible deterioration in catalytic activity during all the studied electrocatalytic reactions such as ORR, MOR, and HER.

Table 4
The HER performance of prepared Pt/HCNFs compared with other related recent reports.

HER Electrocatalysts	Over potential (mV)	Tafel slope (mV dec^{-1})	Mass Activity (A g^{-1})	Ref
Pt/C-5%	NA	40.2	NA	[63]
Pt/C-20%		28.4		
Pt_5/HMCS-5.08%		28.3		
Pt_{Cl}/HMCS-5.08%		34.5		
Pt@Co SAs-ZIF-NC	27	21	0.45 A/mg Pt	[64]
Pt@NPC	15.4	18	NA	[65]
Pt_2Pd/N-doped grahene	58	31	NA	[66]
Pt/vertical graphene nanosheet arrays	60	28	NA	[67]
C_3N_4/AgPt	0.1503 V	65	125.21	[68]
Pt/CQDs/CNT	29	22	NA	[69]
Pt/CF50	NA	128	NA	[59]
Pt/CF100		118	NA	
Pt/CF150		42	2.61 (A/mg)	
Pt/CF300		126	1.67 (A/mg)	
PtNP/rGO-MWCNT	20	NA	10 (mA/μgPt)	[70]
Pt/α-MoC_{1-x}-CNFs-800	133	27	3.49 (A mg^{-1})	[71]
Pt/α-MoC_{1-x}-CNFs-900	73			
Pt/α-MoC_{1-x}-CNFs-1000	38			
Pt/α-MoC_{1-x}-CNFs-1100	50			
Pt/α-MoC_{1-x}-CNFs-1200	68			
Pt/GHSs	27	59.3	NA	[72]
Pt/HCNF-I	51	102	2.314	This
Pt/HCNF-II	38	80	3.419	Work
Pt/HCNF-III	33	54	6.166	
Pt/HCNF-IV	39	77	3.757	
Pt/HCNF-V	62	122	4.993	

Declaration of Competing Interest

The authors declare that they have no known competing financial interests or personal relationships that could have appeared to influence the work reported in this paper.

Acknowledgments

Dr R. Kalai Selvan would like to thank the University Grants Commission (UGC), India, for awarding Raman Post-Doctoral Fellowship to work at North Carolina State University, USA. The work (Synthesis, XPS, and FESEM analysis of HCNF samples) was performed at the Analytical Instrumentation Facility (AIF) at North Carolina State University, USA. Dr S. Shanmugapriya would like to acknowledge DST-PURSE, Phase-II Program, Bharathiar University, to provide a research fellowship. Prof. Yun Sung Lee greatly acknowledged to National Research Foundation of Korea Grant funded by the Korean government (Ministry of Science, ICT and Future Planning) No. 2019R1A2C1007620.

Data availability statement

The raw/processed data required to reproduce these findings cannot be shared at this time due to technical or time limitations.

Appendix A. Supplementary material

Supplementary data to this article can be found online at https://doi.org/10.1016/j.mseb.2022.115880.

References

[1] S. Campisi, C. Edith. C-Thaw, A. Villa, Appl. Sci. 8 (2018) 1159.
[2] L. Shi, S. Liu, Z. He, H. Yuan, J. Shen, Electrochim. Acta 178 (2015) 748–757.
[3] Z. Liu, J. Qu, X. Fu, Q. Wang, G. Zhong, F. Peng, Mater. Lett. 142 (2015) 115–118.
[4] P. Ai, M. Tan, N. Yamane, G. Liu, R. Fan, G. Yang, Y. Yoneyama, R. Yang, N. Tsubaki, Chem. Eur. J. 23 (2017) 8250–8261.
[5] O.Y. Podyacheva, Z.R. Ismagilov, A.I. Boronin, L.S. Kibis, E.M. Slavinskaya, A. S. Noskova, N.V. Shikina, V.A. Ushakov, A.V. Ischenko, Catal Today. 186 (2012) 42–47.
[6] J. Zhu, P. Wei, K. Li, S. He, Z. Pan, S. Nie, J. Key, P.K. Shen, A.C.S. Sustain, Chem. Eng. 7 (2019) 660–668.
[7] R. Yao, J. Gu, H. He, T. Yu, Catalysts 10 (2020) 862.
[8] C.K. Acharya, W. Li, Z. Liu, G. Kwon, C.H. Turner, A.M. Lane, D. Nikles, T. Klein, M. Weaver, J. Power Sources 192 (2009) 324–329.
[9] Q. Shi, C. Zhu, M.H. Engelhard, D. Du, Y. Lin, RSC Adv. 7 (2017) 6303–6308.
[10] Z. Li, Q. Gao, H. Zhang, W. Tian, Y. Tan, W. Qian, Z, Liu, Sci. Rep. 7 (2017) 43352.
[11] Z. Liu, Q. Shi, R. Zhang, Q. Wang, G. Kang, F. Peng, J. Power Sources 268 (2014) 171–175.
[12] M. Li, X. Wu, J. Zeng, Z. Hou, S. Liao, Electrochim. Acta 182 (2015) 351–360.
[13] R. Li, C. Qin, X. Zhang, Z. Lin, S. Lv, X. Jiang, RSC Adv. 9 (9) (2019) 1679–1689.
[14] C. Wang, X. Zhang, J. Wang, Y. Ma, S. Lv, J. Xiang, M. Chu, T. Sun, C. Qin, J. Electrochem. Soc. 165 (2018) A856–A866.
[15] M. G. Rodríguez, O. V. Kharissova, U. O-Méndez, Rev. Adv. Mater. Sci. 7 (2004) 55–60.
[16] S. Wang, J. Feng, Q. Meng, B. Cao, G. Tian, J Solid State Electrochem. 23 (23) (2019) 2377–2390.
[17] L. Zhang, G. Xia, Z. Guo, D. Sun, X. Li, X. Yu, J. Power Sources 324 (2016) 294–301.
[18] T. Liu, M. Li, X. Bo, M. Zhou, J. Colloid Interface Sci. 533 (2019) 709–722.
[19] Q. Xia, H. Yang, M. Wang, M. Yang, Q. Guo, L. Wan, H. Xia, Y. Yu, Adv. Energy Mater. 7 (2017) 1701336.
[20] G. Panomsuwan, N. Saito, T. Ishizaki, Electrochem. Commun. 59 (2015) 81–85.
[21] F. Yang, Y. Cao, Z. Chen, X. He, L. Hou, Y. Li, New J. Chem. 42 (2018) 2718–2725.
[22] Z.-Y. Yu, L.-F. Chen, L.-T. Song, Y.-W. Zhu, H.-X. Ji, S.-H. Yu, Nano Energy 15 (2015) 235–243.
[23] D.J. You, K. Kwon, S.H. Joo, J.H. Kim, J.M. Kim, C. Pak, H. Chang, Int. J. Hydrog. Energy 37 (2012) 6880–6885.
[24] M. Song, Y. Song, H. Li, P. Liu, B. Xu, H. Wei, J. Guo, Y. Wu, Electrochim. Acta 320 (320) (2019) 34603.
[25] G. Zhang, D. Yang, E. Sacher, J. Phys. Chem. C. 111 (2007) 565–570.
[26] R. Siburian, A.M.M. Ali, K. Sebayang, M. Supeno, K. Tarigan, C. Simanjuntak, S. P. Aritonang, F. Hutagalung, Sci. Rep. 11 (2021) 1–13.
[27] D. Higgins, P. Zamani, A. Yu, Z. Chen, Energy Environ. Sci. 9 (2016) 357–390.
[28] S. Shanmugapriya, P.R. Kasturi, P. Zhu, J. Zhu, C. Yan, X. Zhang, R.Kalai Selvan, Sust. Energy Fuels 4 (2020) 2808–2822.
[29] Q. Yang, W. Xu, A. Tomita, T. Kyotani, J. Am. Chem. Soc. 127 (2005) 8956–8957.
[30] K.K. Karuppanan, A.V. Raghu, M.K. Panthalingal, B. Pullithadathil, ChemElectroChem 6 (2019) 2029–2042.
[31] G. Chen, H. Yang, Int. J. Electrochem. Sci. 11 (2016) 34–44.
[32] Y. Garsany, O.A. Baturina, K.E. S-Lyons, S.S. Kocha, Anal. Chem. 82 (2010) 6321–6328.
[33] J. Zhang, Z. Xia, L. Dai, Sci. Adv. 1 (2015) e1500564.
[34] L. Khotseng, Electrocatalysts for fuel cells and hydrogen evolution-theory to design, IntechOpen (2018).
[35] W. Wang, P. Wang, Y. Kang, J. Zhao, P. Tao, Z. Lei, Int. J. Hydrog. Energy 44 (2019) 4771–4779.
[36] C. Alegre, D. Sebastián, M.E. Gálvez, E. Baquedano, R. Moliner, A.S. Aricò, V. Baglio, M.J. Lázaro, Materials 10 (2017) 1092.
[37] J.A. Prithi, N. Rajalakshmi, G.R. Rao, Int. J. Hydrog. Energy 43 (2018) 4716–4725.
[38] Y. Wang, Y. Cai, X. Yan, Z. Kong, Y. Zhang, S. Wang, D. Li, D. Yang, J. Porous Mater. 29 (2022) 1061–1071.
[39] H.G. Jo, K.H. Kim, H.J. Ahn, RSC Adv. 11 (2021) 12209–12217.
[40] M.A. Hoque, F.M. Hassan, A.M. Jauhar, G. Jiang, M.D. Pritzker, J.-Y. Choi, S. Knights, S. Ye, Z. Chen, A.C.S. Sustain, Chem. Eng. 6 (2018) 93–98.
[41] O.L. Li, Z. Shi, H. Lee, T. Ishizaki, Sci. Rep. 9 (2019) 12704.
[42] M. Yi, N. Li, B. Lu, L. Li, Z. Zhu, J. Zhang, Energy Storage Mater. 42 (2021) 418–429.
[43] M. Nadeem, G. Yasin, M. Arif, H. Tabassum, M.H. Bhatti, M. Mehmood, U. Yunus, R. Iqbal, T.A. Nguyen, Y. Slimani, H. Song, W. Zhao, Chem. Eng. J. 409 (2021) 128205.
[44] L. Zhou, Y. Wang, J. Tang, J. Li, S. Wang, Y. Wang, Micropor. Mesopor. Mater. 247 (2017) 116–123.
[45] P. R. Kasturi, R. Kalai Selvan, Y. S. Lee, RSC Adv. 6 (2016) 62680–62694.
[46] Y. Sun, C. Du, G. Han, Y. Qu, L. Du, Y. Wang, G. Chen, Y. Gao, G. Yin, Electrochim. Acta 212 (2016) 313–321.
[47] J. Sun, Y. Ling, Q. Zhang, X. Yu, Z. Yang, RSC Adv 7 (2017) 29839–29843.
[48] Y. Sun, C. Du, M. An, L. Du, Q. Tan, C. Liu, Y. Gao, G. Yin, J. Power Sources 300 (2015) 245–253.
[49] S. Wang, T. Cochell, A. Manthiram, Phys. Chem. Chem. Phys. 14 (2012) 13910–13913.
[50] M. An, C. Du, L. Du, Y. Wang, Y. Wang, Y. Sun, G. Yin, Y. Gao, ChemElectroChem 6 (2019) 1157–1165.
[51] S. Wei, F. Xie, M. Gan, L. Ma, T. Wu, Q. Fu, T. Li, Y. Yang, W. Zhan, Synth. Met. 280 (2021) 116878.

[52] M. Niyaz, N. Sawut, R. Jamal, T. Abdiryim, Z. Helil, H. Liu, S. Xie, Y. Song, Int. J. Hydrogen Energy 46 (2021) 31623–31633.
[53] J.-P. Zhong, C. Hou, L. Li, M. Waqas, Y.-J. Fan, X.-C. Shen, W. Chen, L.-Y. Wan, H.-G. Liao, S.-G. Sun, J. Catal. 381 (2020) 275–284.
[54] K. Huang, J. Zhong, J. Huang, H. Tang, Y. Fan, M. Waqas, B. Yang, W. Chen, J. Yang, Appl. Surf. Sci. 501 (2020) 144260.
[55] K. Peng, N. Bhuvanendran, S. Ravichandran, Z. Xu, W. Zhang, Q. Ma, Q. Xu, L. Khotseng, H. Su, Int. J. Hydrog. Energy 45 (2020) 9795–9802.
[56] M.S. Cogenli, A.B. Yurtcan, Int. J. Hydrog. Energy 45 (2020) 650–666.
[57] S. Ravichandran, N. Bhuvanendran, Q. Xu, T. Maiyalagan, H. Su, Electrochim. Acta 394 (2021) 139148.
[58] A.H. Ghanim, J.G. Koonce, B. Hasa, A.M. Rassoolkhani, W. Cheng, D.W. Peate, J. Lee, S. Mubeen, Front. Chem. 6 (2018) 523.
[59] B. Jiang, F. Liao, Y. Sun, Y. Cheng, M. Shao, Nanoscale 9 (2017) 10138–10144.
[60] F. Davodi, M. Tavakkoli, J. Lahtinen, T. Kallio, J. Catal. 353 (353) (2017) 19–27.
[61] Y. Liu, H. Yu, X. Quan, S. Chen, H. Zhao, Y. Zhang, Sci. Rep. 4 (2014) 6843.
[62] L. Zhang, J. Lu, S. Yin, L. Luo, S. Jing, A. Brouzgou, J. Chen, P.K. Shen, P. Tsiakaras, Appl. Catal. B-Environ. 230 (2018) 58–64.
[63] X.-K. Wan, H.B. Wu, B.Y. Guan, D. Luan, X.W.D. Lou, Adv. Mater. 32 (2020) 1901349.
[64] L. Liang, H. Jin, H. Zhou, B. Liu, C. Hu, D. Chen, Z. Wang, Z. Hu, Y. Zhao, H.W. Li, D. He, S. Mu, Nano Energy 88 (2021) 106221.
[65] Y. Dong, J. Ying, Y.X. Xiao, J.B. Chen, X.Y. Yang, Chem. - An Asian J. 16 (2021) 1878–1881.
[66] X. Zhong, Y. Qin, X. Chen, W. Xu, G. Zhuang, X. Li, J. Wang, Carbon 114 (2017) 740–748.
[67] H. Zhang, W. Ren, C. Guan, C. Cheng, J. Mater. Chem. A 5 (2017) 22004.
[68] R. Nazir, P. Fageria, M. Basu, S. Pande, J. Phys. Chem. C 121 (2017) 19548–19558.
[69] J. Liang, Y. Liu, R. Liu, S. Zheng, Z. Si, D. Weng, F. Kang, Nano Sel. 2 (2021) 2126–2134.
[70] D. Zhou, B. Jiang, R. Yang, X. Hou, C. Zheng, Chin. Chem. Lett. 31 (2020) 1540–1544.
[71] X. Pan, S. Lu, D. Zhang, Y. Zhang, F. Duan, H. Zhu, H. Gu, S. Wang, M. Du, J. Mater. Chem. A 8 (2020) 4911–4919.
[72] C. Fan, X. Jiang, J. Chen, X. Wang, S. Qian, C. Zhao, L. Ding, D. Sun, Y. Tang, Small Struct. 2 (2021) 2000017.
[73] C.G. Vayenas, S. Bebelis, C. Pliangos, S. Brosda, D. Tsiplakides, Electrochemical Activation of Catalysis: Promotion, Electrochemical Promotion, and Metal-Support Interactions, Springer Science & Business Media, NY, USA, 2001.